Research article

Dongyi Wang, Tong Liu, Yuejiao Zhou, Xiaoying Zheng, Shulin Sun, Qiong He* and Lei Zhou*

High-efficiency metadevices for bifunctional generations of vectorial optical fields

https://doi.org/10.1515/nanoph-2020-0465
Received August 9, 2020; accepted September 16, 2020; published online October 8, 2020

Abstract: Vectorial optical fields (VOFs) exhibiting tailored wave fronts and spatially inhomogeneous polarization distributions are particularly useful in photonic applications. However, devices to generate them, made by natural materials or recently proposed metasurfaces, are either bulky in size or less efficient, or exhibit restricted performances. Here, we propose a general approach to design metadevices that can efficiently generate two distinct VOFs under illuminations of circularly polarized lights with different helicity. After illustrating our scheme via both Jones matrix analyses and analytical model calculations, we experimentally demonstrate two metadevices in the near-infrared regime, which can generate vortex beams carrying different orbital angular momenta yet with distinct inhomogeneous polarization distributions. Our results provide an ultracompact platform for bifunctional generations of VOFs, which may stimulate future works on VOF-related applications in integration photonics.

Keywords: bifunctional metasurfaces; local polarization distributions; Pancharatnam–Berry phase; resonance phase; spin-decoupled functionalities; vectorial optical fields.

1 Introduction

Vectorial optical fields (VOFs) are special solutions of Maxwell's equations, which exhibit well-defined wave fronts and tailored inhomogeneous distributions of polarization (also called "spin") state [1, 2]. The latter, unique to electromagnetic (EM) waves being vectorial in nature, make VOFs particularly useful in many applications such as optical communications, biosensing and chemical sensing, particle trapping and high-resolution imaging [2, 3]. However, conventional approaches to generate VOFs require separate devices to control wave fronts (e.g., spatial light modulators [4]) and inhomogeneous polarization distributions (e.g., Q-plate [5] or spiral phase elements [6]) of light, which are bulky and complicated. Moreover, usually a single system can only generate a particular VOF. All these limitations make conventional devices unfavorable for integration photonics applications.

Metasurfaces, ultrathin metamaterials composed by planar subwavelength microstructures (e.g., meta-atoms) exhibiting tailored optical properties, attracted immense interests recently owing to their unprecedented capabilities to control EM waves [7–9]. Designing metasurfaces to exhibit certain anisotropic or spatially inhomogeneous phase distributions for reflected/transmitted waves, researchers have demonstrated separate manipulations on polarization [10–12] or wave front [13–18] properties of EM waves, leading to many practical applications (e.g.,

Dongyi Wang, Tong Liu, and Yuejiao Zhou contributed equally to this work.

***Corresponding authors: Qiong He and Lei Zhou**, State Key Laboratory of Surface Physics, Key Laboratory of Micro and Nano Photonic Structures (Ministry of Education) and Department of Physics, Fudan University, Shanghai 200438, China; Academy for Engineering and Technology, Fudan University, Shanghai 200433, China; and Collaborative Innovation Centre of Advanced Microstructures, Nanjing 210093, China, E-mail: qionghe@fudan.edu.cn (Q. He), phzhou@fudan.edu.cn (L. Zhou)
Dongyi Wang, Tong Liu, Yuejiao Zhou and Xiaoying Zheng, State Key Laboratory of Surface Physics, Key Laboratory of Micro and Nano Photonic Structures (Ministry of Education) and Department of Physics, Fudan University, Shanghai 200438, China, E-mail: dywang17@fudan.edu.cn (D. Wang), tongliu16@fudan.edu.cn (T. Liu), 18110190015@fudan.edu.cn (Y. Zhou), 18110190014@fudan.edu.cn (X. Zheng). https://orcid.org/0000-0002-8947-707X (T. Liu)
Shulin Sun, Shanghai Engineering Research Centre of Ultra-Precision Optical Manufacturing, Green Photonics and Department of Optical Science and Engineering, Fudan University, Shanghai 200433, China, E-mail: sls@fudan.edu.cn. https://orcid.org/0000-0003-3046-1142

polarization control [10–12], light-bender [13–17], metalens [19–23], and metahologram [24–27]). More recently, metadevices exhibiting combined functionalities of polarization and wave front manipulations were proposed [18, 28–39], some of which could already generate particular VOFs as desired [29–31, 37–43] These devices are generally flat and ultracompact, being very promising for on-chip photonic applications.

Despite of the fast developments along this research direction, several limitations still hinder the practical applications of these VOF metagenerators. First of all, metadevices so far proposed can usually generate only one particular VOF [18, 30, 31, 38, 40–42], while multifunctional VOF generators are highly desired in future applications. Secondly, most reported metadevices can only generate VOFs with restricted polarization distributions (e.g., standard cylindrical polarization distributions [18, 31, 39, 44–46]), while VOFs with *arbitrary* polarization distributions are rarely seen. The inherent physics behind such issues are that previous approaches only utilized a single mechanism (either resonance or geometric mechanism) to design meta-atoms in constructing metadevices and only explored certain polarization-control capabilities of the constitutional meta-atoms [28–32, 38, 45–49]. Although some sporadic works have reported the VOF generations employing multiple mechanisms [46, 50], few of those designs was demonstrated experimentally in optical regime.

In this paper, we propose a generic approach to design metadevices that can efficiently generate two distinct VOFs with *designable* polarization distributions, upon excitations of circularly polarized (CP) lights with two opposite helicity. We achieve this end by choosing meta-atoms possessing reflection phases governed by two different mechanisms (resonance and geometric ones) and taking *full* use of the polarization-control capabilities of constitutional meta-atoms. After explaining the basic concept with Jones matrix analyses, we explicitly illustrate our strategy based on analytical Green's function (GF) calculations. As the proof of our concept, we experimentally demonstrate two metadevices working at telecom wavelengths, which can achieve bifunctional generations of distinct VOFs exhibiting vortex wave fronts with different orbital angular momenta (OAM) and inhomogeneous polarization distributions including standard and more general ones. We finally discuss potential applications of our strategy and present our own perspectives on possible future works, before concluding this paper.

2 Results and discussions

2.1 Basic concept

We start from discussing the phase distributions required by our metadevices, which are supposed to be able to generate two distinct VOFs under illuminations of CP lights with different helicity (see Figure 1b). In this paper, we study reflective metasurfaces as an example to illustrate our key idea and extensions to the transmissive case are straightforward. To realize such spin-delinked dual functionalities, our meta-atoms should exhibit both spin-*dependent* geometric phases and spin-*independent* resonant phases, as already pointed out in recent literature [33, 35, 39, 46, 51, 52]. Moreover, to generate a predesigned polarization distribution in the VOF, our meta-atoms should further possess desired local polarization-control capabilities, corresponding to certain paths on Poincare's sphere (see Figure 1a).

Based on the above two requirements, we consider a generic reflective meta-atom exhibiting mirror symmetries with respect to two principle axes denoted as u and v, which is then rotated by an angle ξ with respect to the laboratory coordinate system (see inset to Figure 1a). Jones matrix of such a meta-atom can be written as $\mathbf{R} = \mathbf{M}(\xi)\begin{pmatrix} r_{uu} & 0 \\ 0 & r_{vv} \end{pmatrix}\mathbf{M}^{-1}(\xi)$ in linear polarization (LP) bases in laboratory coordinate system, where $\mathbf{M}(\xi) = \begin{pmatrix} \cos\xi & -\sin\xi \\ \sin\xi & \cos\xi \end{pmatrix}$, $r_{uu} = e^{i\Phi_u}$ and $r_{vv} = e^{i\Phi_v}$. Here, we neglect material losses as we establish the theoretical framework, and later we show that adding losses back does not significantly change the established picture. Transform the bases from LP ones to CP ones, the resulting Jones matrix reads $\tilde{\mathbf{R}} = \mathbf{S}\mathbf{R}\mathbf{S}^{-1}$ with $\mathbf{S} = \frac{\sqrt{2}}{2}\begin{pmatrix} 1 & -i \\ 1 & i \end{pmatrix}$ [48, 49]. Shine such a meta-atom by CP light exhibiting different spin $|\sigma\rangle$ with $|+\rangle = \begin{pmatrix} 1 \\ 0 \end{pmatrix}$ and $|-\rangle = \begin{pmatrix} 0 \\ 1 \end{pmatrix}$ denoting left circular polarization (LCP) and right circular polarization (RCP), respectively, we find that the reflected wave becomes

$$\tilde{\mathbf{R}}|\sigma\rangle = e^{i\Phi^{\sigma}_{\mathrm{ini}}}|f^{\sigma}\rangle. \tag{1}$$

Here, $|f^{\sigma}\rangle = \begin{pmatrix} e^{-i\Psi^{\sigma}/2}\cos(\Theta^{\sigma}/2) \\ e^{i\Psi^{\sigma}/2}\sin(\Theta^{\sigma}/2) \end{pmatrix}$ denotes the polarization state of the reflected wave represented by a point $(\Theta^{\sigma}, \Psi^{\sigma})$ on Poincare's sphere and $\Phi^{\sigma}_{\mathrm{ini}}$ is the initial phase carried by

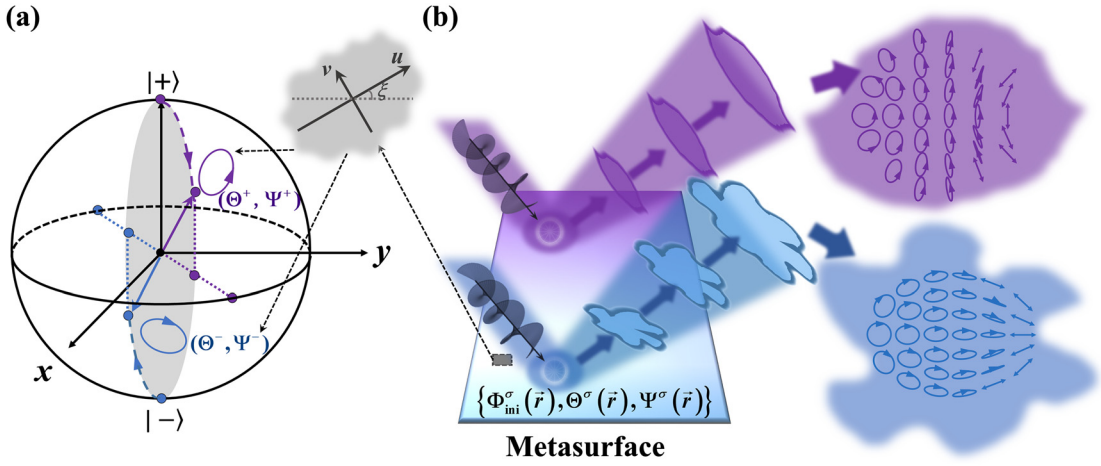

Figure 1: Schematics of spin-delinked bifunctional vectorial optical field (VOF) generations.
(a) Dashed lines in blue and purple colors illustrate how the polarization change from initial left circular polarization (LCP) and right circular polarization (RCP) states to two final states denoted by two points (Θ^+, Ψ^+) and (Θ^-, Ψ^-) on Poincare's sphere, as our meta-atom is shined by incident CP light with different helicity. Inset to (a) illustrates the local coordinate of a meta-atom. (b) Schematics of light scatterings at a metasurface exhibiting pre-designed distributions of $\{\Phi^\sigma_{\rm ini}(\vec{r}), \Theta^\sigma(\vec{r}), \Psi^\sigma(\vec{r})\}$ under LCP and RCP illuminations, generating two distinct reflected beams with different wave fronts and inhomogeneous polarization distributions.

the reflected wave. It is worth noting that two angles $(\Theta^\sigma, \Psi^\sigma)$ unambiguously determine the polarization state, with $\cos\Theta^\sigma$ representing the ellipticity and $\Psi^\sigma/2$ dedicating the polar angle of the polarization.

This set of parameters, $\{\Theta^\sigma, \Psi^\sigma, \Phi^\sigma_{\rm ini}\}$, are determined by the properties of our meta-atoms $\{\Phi_u, \Phi_v, \xi\}$. For the cases of $\Delta\Phi = \Phi_v - \Phi_u \neq \pm\pi$, we find

$$\begin{cases} \Theta^+ = \Delta\Phi, & \Psi^+ = 2\xi - \dfrac{\pi}{2} \\ \Theta^- = \pi - \Delta\Phi, & \Psi^- = 2\xi + \dfrac{\pi}{2} \end{cases} \tag{2}$$

and

$$\Phi^\sigma_{\rm ini} = \Phi_{\rm res} + \sigma \cdot \Phi_{\rm geo} \tag{3}$$

where $\Phi_{\rm res} = \overline{\Phi} - \pi/4$ (with $\overline{\Phi} = (\Phi_u + \Phi_v)/2$) is a spin-*independent* term originated from structural resonances and $\Phi_{\rm geo} = \xi$ is a spin-*dependent* term originated from the geometric effect (e.g., structural rotation). The case of $\Delta\Phi = \pm\pi$ corresponds to a singular point in the gauge that we choose here, and $\Psi^\sigma, \Phi_{\rm res}, \Phi_{\rm geo}$ take different expressions:

$$\Psi^\sigma = 0\,; \quad \Phi_{\rm res} = \arg\left(e^{i\Phi_u} - e^{i\Phi_v}\right); \quad \Phi_{\rm geo} = 2\xi\,. \tag{4}$$

Equations (1)–(4) contain the crucial physics presented in this paper. After reflections by such a meta-atom, the polarization of light can change from the initial LCP or RCP to different final states represented by $(\Theta^\sigma, \Psi^\sigma)$ (see Figure 1a). Meanwhile, initial phases $\Phi^\sigma_{\rm ini}$ carried by waves reflected by different meta-atoms under different CP excitations are useful for constructing VOFs exibiting predesigned wave fronts (see Figure 1b). Therefore, if we choose a set of meta-atoms with appropriate scattering properties to form a metasurface exhibiting certain $\Theta^\sigma(\vec{r})$, $\Psi^\sigma(\vec{r})$ and $\Phi^\sigma_{\rm ini}(\vec{r})$ distributions, we can thus realize bifunctional generations of VOFs with different wave fronts (dictated by $\Phi^\sigma_{\rm ini}(\vec{r})$) and polarization distributions (dictated by $\Theta^\sigma(\vec{r})$, $\Psi^\sigma(\vec{r})$) as shining the metasurface by CP lights with different spin.

Before closing this sub-section, we discuss several important physics. First of all, the presence of both spin-*independent* $\Phi_{\rm res}$ and spin-*dependent* $\Phi_{\rm geo}$ in Eq. (3) is crucial to construct two *discorrelated* phase distributions (i.e., $\Phi^+_{\rm ini}(\vec{r})$ and $\Phi^-_{\rm ini}(\vec{r})$), making spin-delinked bifunctional controls possible. Secondly, varying $\Delta\Phi$ and ξ can *continuously* change the polarization state of the reflected wave (see Eq. (2)), which is crucial to realize desired inhomogeneous polarization distributions. Thirdly, we note that for the cases of $\Delta\Phi \neq \pm\pi$, the geometric phase $\Phi_{\rm geo} = \xi$ does not exhibits the standard Pancharatnam–Berry (PB) form (i.e., $\Phi_{\rm PB} = 2\xi$ [48, 53–56]). The underlying physics is that the final spin states in such cases carry a phase factor $e^{i\xi}$, which is different from the special case of $\Delta\Phi = \pm\pi$. More discussions on this point are presented in Sec. 1 of Supplementary material (SM).

Finally, we discuss the limitations of our proposed bifunctional VOF generations. Since the meta-atoms we choose here only exhibit three independent parameters (i.e., Φ_u, Φ_v and ξ, or equivelantly, $\Delta\Phi$, $\Phi_{\rm res}$ and ξ), they can *not* be used to realize metasurfaces with *freely* designable

$\Theta^{\sigma}(\vec{r})$, $\Psi^{\sigma}(\vec{r})$ and $\Phi^{\sigma}_{\mathrm{ini}}(\vec{r})$ functions which require six free parameters. In fact, Eq. (2) shows that $(\Theta^{+}(\vec{r}), \Psi^{+}(\vec{r}))$ are inherently correlated with $(\Theta^{-}(\vec{r}), \Psi^{-}(\vec{r}))$, indicating that the resulting polarization distributions of two VOFs are ultimately connected. Also, once the two initial phase distributions ($\Phi^{+}_{\mathrm{ini}}(\vec{r})$ and $\Phi^{-}_{\mathrm{ini}}(\vec{r})$) are predetermined, we find from Eq. (3) that the function $\Phi_{\mathrm{geo}}(\vec{r})$ is also fixed, which subsequently locks the $\Psi^{\pm}(\vec{r})$ functions determining the polar angles of polarizations. In practical designs, we usually only pre-determine three functions $\{\Phi^{+}_{\mathrm{ini}}(\vec{r}), \Phi^{-}_{\mathrm{ini}}(\vec{r}), \Theta^{+}(\vec{r})\}$ from all six ones, since the remaining three ones (i.e., $\{\Theta^{-}(r^{\rightarrow}), \Psi^{+}(r^{\rightarrow}), \Psi^{-}(r^{\rightarrow})\}$) are automatically determined by $\{\Phi^{+}_{\mathrm{ini}}(\vec{r}), \Phi^{-}_{\mathrm{ini}}(\vec{r}), \Theta^{+}(\vec{r})\}$ as shown in Eqs. (2)–(4). We emphasize that the designable distributions of $\Theta^{+}(\vec{r})$ enable the full control on both local ellipticity and inhomogeneous helicity.

2.2 Verifications by GF calculations on an ideal model

We now illustrate how to implement our strategy based on GF calculations on an ideal model. As a particular example, we choose to generate two divergent vectorial vortex beams carrying different OAMs (with topological charges $l = 2$ and $l = 0$, respectively) and exhibiting distinct polarization distributions (see Figures 2a and d). To achieve this goal, we assume that:

$$\begin{cases} \Phi^{+}_{\mathrm{ini}}(\vec{r}) = 2\pi\dfrac{r}{P_s} + 2\varphi \\ \Phi^{-}_{\mathrm{ini}}(\vec{r}) = 2\pi\dfrac{r}{P_s} - \dfrac{\pi}{2} \\ \Theta^{+}(\vec{r}) = \begin{cases} \varphi & 0 \le \varphi < \pi \\ 2\pi - \varphi & \pi \le \varphi < 2\pi \end{cases} \end{cases} \tag{5}$$

where $P_s = 1.55\lambda$ with λ being the working wavelength. φ and r are the polar angle and radius of a vector $\vec{r}$ in cylindrical coordinate system. Based on the correlations set up in Eqs. (2) and (3), we can readily retrieve the remaining three functions

$$\begin{cases} \Theta^{-}(\vec{r}) = \begin{cases} \pi - \varphi & 0 \le \varphi < \pi \\ \varphi - \pi & \pi \le \varphi < 2\pi \end{cases} \\ \Psi^{+}(\vec{r}) = 2\varphi \\ \Psi^{-}(\vec{r}) = 2\varphi + \pi \end{cases} \tag{6}$$

Equations (5) and (6) reveal the properties of two VOFs to be generated. The first two lines in Eq. (5) suggest that two reflected beams exhibit vortex wave fronts carrying

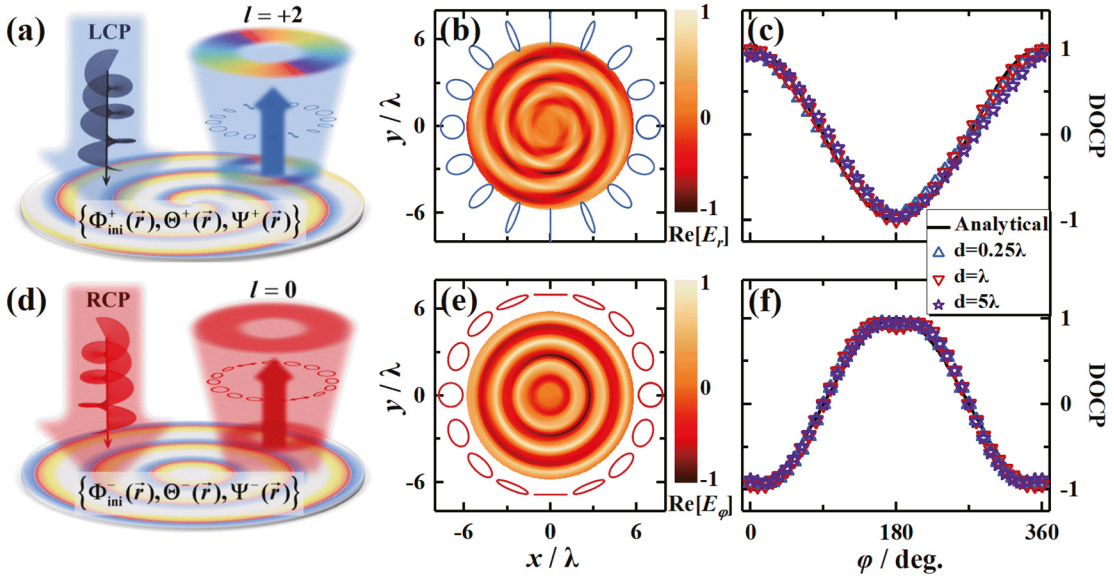

Figure 2: Analytical calculations on a model system.
Schematics of light scatterings by a model metasurface exhibiting $\{\Phi^{\sigma}_{\mathrm{ini}}(\vec{r}), \Theta^{\sigma}(\vec{r}), \Psi^{\sigma}(\vec{r})\}$ distributions as given by Eqs. (5) and (6), under illuminations of (a) left circular polarization (LCP) and (d) right circular polarization (RCP) incidences. (b) Re$[E_r]$ distribution on an *xy* plane at a distance $d = \lambda$ above the metasurface for reflected beam under LCP incidence, and (e) Re$[E_{\varphi}]$ distribution on an *xy* plane at a distance $d = \lambda$ above the metasurface for reflected beam under RCP incidence, calculated by the Green's function approach. Ellipses illustrate the polarization patterns at different angles. Degrees of circular polarization as functions of the azimuthal angle φ, calculated by the Green's function approach for reflected waves on *xy* planes at different distances (denoted by *d*) above the metasurface under (c) LCP and (f) RCP incidences, respectively. Solid lines in (c) and (f) are directly obtained from the final polarizations defined by Eqs. (5) and (6).

different topological charges. Meanwhile, the third line in Eq. (5) and the first line in Eq. (6) indicate that the ellipticity of local polarization changes dramatically inside two reflected beams. Finally, the last two lines in Eq. (6) imply that polar angle of local polarization also changes as varying φ, which are along the radial and tangential directions for the cases of LCP and RCP incidences, respectively.

With Eq. (5) known, we numerically retrieve the scattering properties of all meta-atoms according to Eqs. (2)–(4), represented by the $\Phi_u(\vec{r})$, $\Phi_v(\vec{r})$ and $\xi(\vec{r})$ distributions. Knowing these information, we then employ the standard GF approach to study the beams reflected by our model system, simply replacing each meta-atom by appropriate oscillating surface current yielding the same scattered field (see Sec. 2 in SM for more details). Figures 2b and e depict, respectively, the distributions of scattered $\mathrm{Re}[E_r]$ and $\mathrm{Re}[E_\varphi]$ on a plane $d = \lambda$ above the metasurface, as it is shined by CP lights with different spin. We could clearly see that the reflected beams exhibit OAM features with topological charges $l = 2$ and $l = 0$, respectively. Meanwhile, we also calculated the polarization patterns at different local points inside the reflected beams and then schematically illustrated in Figures 2b and e how the polarization changes along the azimuthal angle (see those ellipses surrounding the patterns). Quantatively, we depict in Figures 2c and f how the local degree of circular polarization (DOCP), defined as $\mathrm{DOCP} = \left(\left|E_r - iE_\varphi\right|^2 - \left|E_r + iE_\varphi\right|^2\right)/\left(\left|E_r - iE_\varphi\right|^2 + \left|E_r + iE_\varphi\right|^2\right)$, vary against the azimuthal angle φ, on xy planes at different distances above the metasurface. These results clearly show that the generated inhomogeneous polarization distribution preserves well as the beams propagate in air, in consistency with our analytical predictions (solid lines in Figure 2c and f) based on the predetermined $(\Theta^{\pm}(\vec{r}), \Psi^{\pm}(\vec{r}))$ functions. Details on the GF approach and more analytical results can be found in Sec. 2 of SM.

2.3 Meta-atom designs

We now choose the near infrared (NIR) regime to experimentally demonstrate our idea, starting from designing appropriate meta-atoms. As shown in the inset to Figure 3a, our basic meta-atom is in metal-insulator-metal (MIM) configuration, which consists of a gold (Au) cross-shaped resonator (with principle axes rotated by an angle ξ) and a continuous 125-nm-thick Au film separated by a 100-nm-thick SiO_2 spacer. Such an MIM meta-atom can reflect incident lights polarized along two principle axes efficiently (100% in ideal lossless cases), with reflection phases Φ_u and Φ_v dictated by two bar-lengths L_u and L_v.

We perform finite-difference time-domain (FDTD) simulations to study how Φ_u and Φ_v vary against L_u and L_v at the working wavelength of 1550 nm, with material losses fully taken into account. Figure 3a shows that Φ_u sensitively depends on L_u and varying L_u can drive Φ_u to near cover the whole 2π range, manifesting a typical magnetic resonance behavior [57]. Meanwhile, Φ_v exhibits a similar dependence on L_v (see more simulation results in Fig. S4 in SM). For the benefits of future designs, we further depict in Figures 3b and c how Φ_{res} and $\Delta\Phi$ vary against L_u and L_v, respectively. There results can help us quickly sort out the geometric parameters (L_u, L_v) and orientation angle of meta-atoms located at different points, from the $\{\Phi_{\mathrm{res}}(\vec{r}), \Delta\Phi(\vec{r}), \xi(\vec{r})\}$ distributions retrieved from the pre-determined $\{\Phi^{+}_{\mathrm{ini}}(\vec{r}), \Phi^{-}_{\mathrm{ini}}(\vec{r}), \Theta^{+}(\vec{r})\}$ distributions.

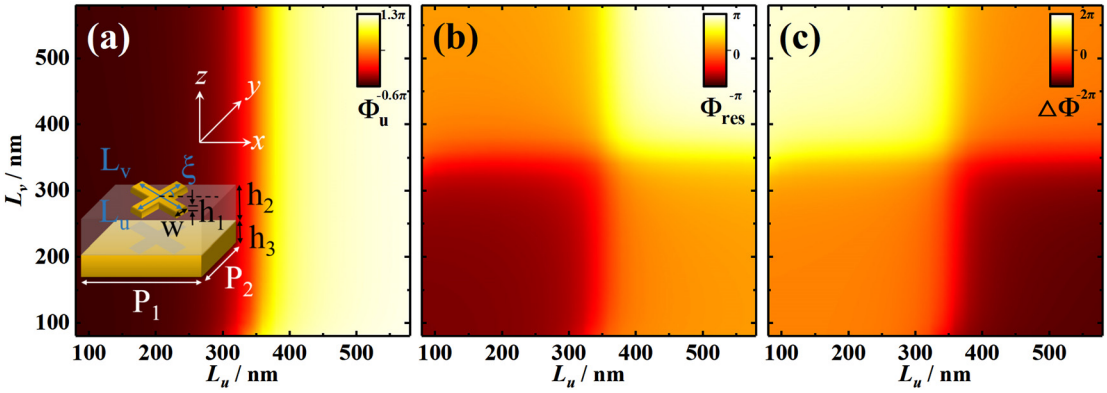

Figure 3: Meta-atom designs at the wavelength of 1550 nm.
(a) finite-difference time-domain (FDTD)–computed reflection phase Φ_u versus L_u and L_v for meta-atoms (see inset) under illuminations of $\hat{u}$-polarized light. Other geometrical parameters of the meta-atoms are fixed as $h_1 = 30$ nm, $h_2 = 100$ nm, $h_3 = 125$ nm, $w = 80$ nm, and $P_1 = P_2 = 600$ nm. (b) Resonance phase Φ_{res} and (c) cross-polarization phase difference $\Delta\Phi$ versus L_u and L_v, computed by FDTD simulations for our meta-atoms. The working wavelength is set as 1550 nm.

2.4 Experimental demonstrations

2.4.1 Metadevice I: bifunctional generations of cylindrically polarized beams

We now experimentally verify our concept, starting from demonstrating the most standard VOFs exhibiting cylindrical polarizations. Without losing generality, we assume our metadevice to exhibit the following distributions:

$$\Phi^{+}_{\mathrm{ini}}(\vec{r}) = 3\varphi\,; \quad \Phi^{-}_{\mathrm{ini}}(\vec{r}) = \varphi - \frac{\pi}{2}; \quad \Theta^{+}(\vec{r}) = \frac{\pi}{2} \tag{7}$$

which, based on the inherent restrictions set in Eqs. (2) and (3), yield the following explicit forms of the remaining three functions :

$$\Theta^{-}(\vec{r}) = \frac{\pi}{2}; \quad \Psi^{+}(\vec{r}) = 2\varphi\,; \quad \Psi^{-}(\vec{r}) = 2\varphi + \pi \tag{8}$$

Equations (7) and (8) clearly reveal the expected properties of two VOFs to be generated. Distributions of $(\Phi^{+}_{\mathrm{ini}}(\vec{r}), \Phi^{-}_{\mathrm{ini}}(\vec{r}))$ in Eq. (7) indicate that two reflected beams are of vortex wave fronts carrying different topological charges ($l = 3$ and $l = 1$, see Figures 4a and b). Yet, $\Theta^{+}(\vec{r}) = \Theta^{-}(\vec{r}) = \pi/2$ dictates that all local spin states inside the two reflected beams should be LPs. Finally, $\Psi^{+}(\vec{r})$ and $\Psi^{-}(\vec{r})$ distributions in Eqs. (7) and (8) suggest that the polar directions of these LPs are along the radial or tangential directions, respectively, for two different input spins.

Following the strategy described in last subsection, we first retrieve from Eqs. (7) and (8) the distributions of $\{\Phi_{\mathrm{res}}(\vec{r}), \Delta\Phi(\vec{r}), \xi(\vec{r})\}$, which further assist us to determine the geometric parameters of all meta-atoms $\{L_u(\vec{r}), L_v(\vec{r}), \xi(\vec{r})\}$ based on Figures 3b and c. We finally design and fabricate out the sample (see scanning electron microscopy (SEM) pictures in Figures 4c and d) according to these parameter distributions, and characterize the scattering properties of this sample (Figure 5).

Figures 5a–c illustrate the essential properties of the beam reflected by our metadevice under LCP plane wave excitation. To clearly characterize the vortex properties of the generated VOF, we perform interference measurement with a homemade Michelson interferometer. Interference between the generated VOF and an incident spherical wave yields a 3rd-order spiral shape in the interference pattern (see dashed lines in Figure 5a), which is the clear evidence of an $l = 3$ vortex. Interferences with a plane wave reinforced our conclusion (see Figs. S5 in SM). We now experimentally characterize the polarization distribution of the generated VOF. Placing a linear polarizer in front of our charge-coupled device (CCD), we find that the recorded intensity image changes dramatically as we rotate the polarizer, visualizing the desired inhomogeneous polarization distribution as expected (see Figs. S6

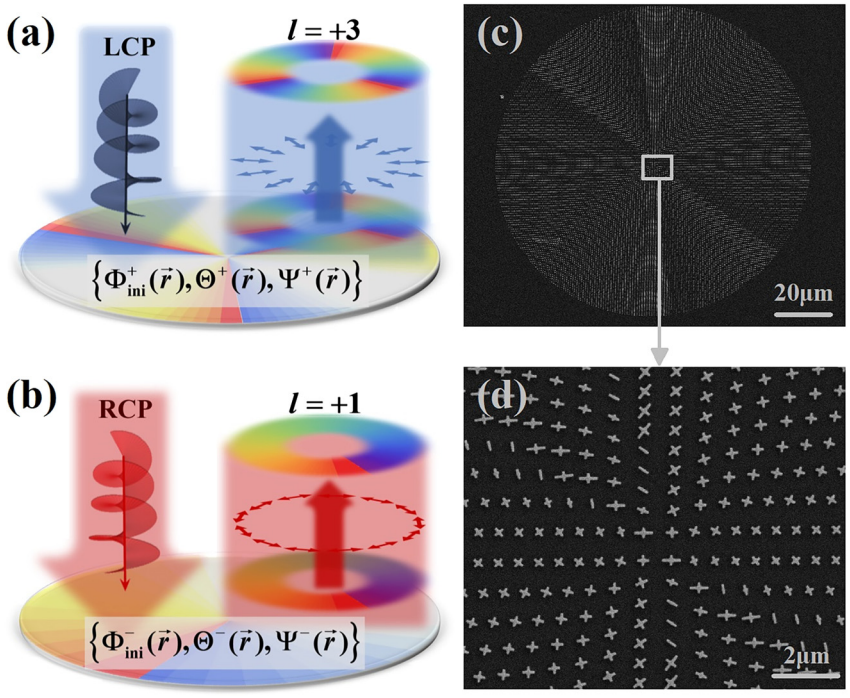

Figure 4: Expected bifunctionalities of metadevice I and its sample picture. Schematics of light scatterings at a metadevice exhibiting $\{\Phi^{+}_{\mathrm{ini}}, \Theta^{+}, \Psi^{+}\}$ and $\{\Phi^{-}_{\mathrm{ini}}, \Theta^{-}, \Psi^{-}\}$ distributions as given by Eqs. (7) and (8), under illuminations of (a) left circular polarization (LCP) and (b) right circular polarization (RCP) incidences. (c) Scanning electron microscopy (SEM) image and (d) a zoom-in view of the fabricated sample.

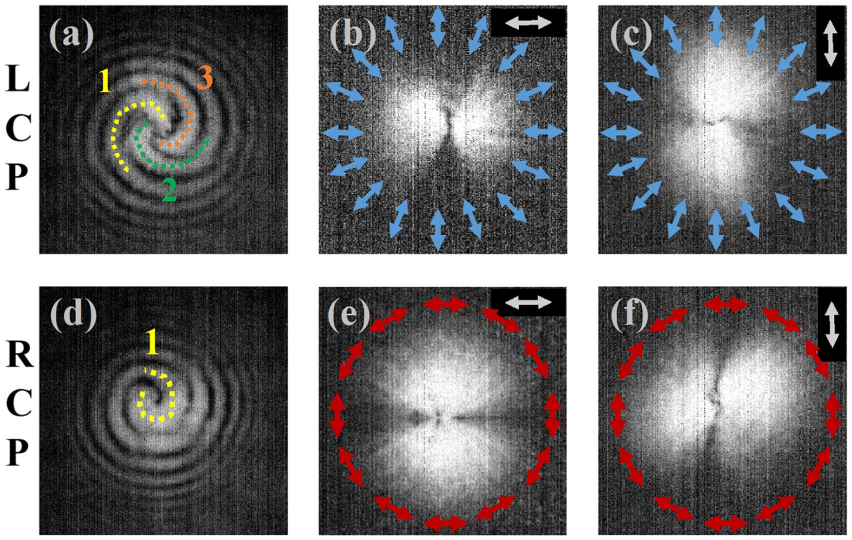

Figure 5: Experimental characterizations on metadevice I.
Measured far-field interference patterns between a spherical reference wave and light beams reflected by metadevice I under (a) left circular polarization (LCP) and (d) right circular polarization (RCP) incidences, respectively. Far-field images recorded by our charge-coupled device (CCD) with a linear polarizer placed in front of it, tilted by an angle of (b, e) 0° and (c, f) 90°, as metadevice I is illuminated by (b, c) LCP and (e, f) RCP incidences, respectively. Arrows in (b, c, e, f) illustrate the expected polarization patterns at different angles.

in SM). In particular, the image profile obtained with our polarizer placed horizontally (Figure 5b) or vertically (Figure 5c) exhibits a nice donut shape with intensity zeros appearing at the angles perpendicular to the polarizer, well illustrating the radial polarization distribution as expected.

Under the RCP incidence, however, both wave front and polarization distribution of the reflected beam change dramatically. Now the interference pattern contains a 1st-order spiral shape indicating that $l = 1$ (Figure 5d), in consistency with our expectation. Meanwhile, repeating the intensity measurements with a rotating polarizer, we find that now the intensity zeros appear at the directions parallel to the polarizer (Figures 5e and f), indicating that now the polarization distribution changes to a tangentially polarized one, as expected. More experimental results can be found in Sec. 4 of SM.

Since it is difficult to experimentally characterize the working efficiency of our metadevice due to the technical limitation of our experimental setup, the highly inhomogeneous polarization distribution of generated VOFs and the presence of undesired stray light, we numerically estimate it as an average of efficiencies of all individual meta-atoms constructing our metadevice. Due to material loss which is the only reason, the efficiency of our metadevices is limited to 55% at working wavelength but still comparable to those of recent PB metadevices at different working frequencies [25, 48, 56]. We emphasize that the working efficiency of our metadevices can be further improved to 100% by constructing our meta-atoms with less lossy materials (e.g. dielectric resonators) (see Section 7 in SM).

2.4.2 Metadevice II: bifunctional generations of vectorial beams beyond cylindrical polarizations

We proceed to experimentally demonstrate another device, which, upon excitations of CP lights with different spin, can generate vectorial beams with polarization distributions *beyond* the standard cylindrical ones. Explicitly, we require metadevice II to exhibit the following expressions for the chosen three functions:

$$\Phi^{+}_{\mathrm{ini}}(\vec{r}) = 3\varphi\,; \quad \Phi^{-}_{\mathrm{ini}}(\vec{r}) = -\varphi - \frac{\pi}{2}; \quad \Theta^{+}(\vec{r}) = \frac{\pi}{2}. \tag{9}$$

According to Eqs. (2)–(4), we immediately obtain the forms of remaining functions:

$$\Theta^{-}(\vec{r}) = \frac{\pi}{2}; \quad \Psi^{+}(\vec{r}) = 4\varphi\,; \quad \Psi^{-}(\vec{r}) = 4\varphi + \pi \tag{10}$$

Compared to Eqs. (7) and (8), the most crucial difference is that, for this device, the orientations of local LPs are no longer along $\hat{e}_r$ and $\hat{e}_\varphi$ directions, as revealed by its $\{\Psi^{+}(\vec{r}), \Psi^{-}(\vec{r})\}$ distributions. Meanwhile, two reflected beams still exhibit vortex wave fronts but with topological charges $l = 3$ and $l = -1$, respectively. Figures 6a and e schematically depict the expected wave front and polarization properties of beams reflected by metadevice II under LCP and RCP incidences, respectively. Following the design strategy as discussed in Sec. 2.3, we successfully retrieve from Eqs. (9) and (10) the geometric parameters $\{L_u(\vec{r}), L_v(\vec{r}), \xi(\vec{r})\}$ of all needed meta-atoms, which help us to finally fabricate out the sample (see Fig. S11 in SM for its SEM picture).

We perform experiments similar to those in last subsection to characterize the essential properties of two reflected

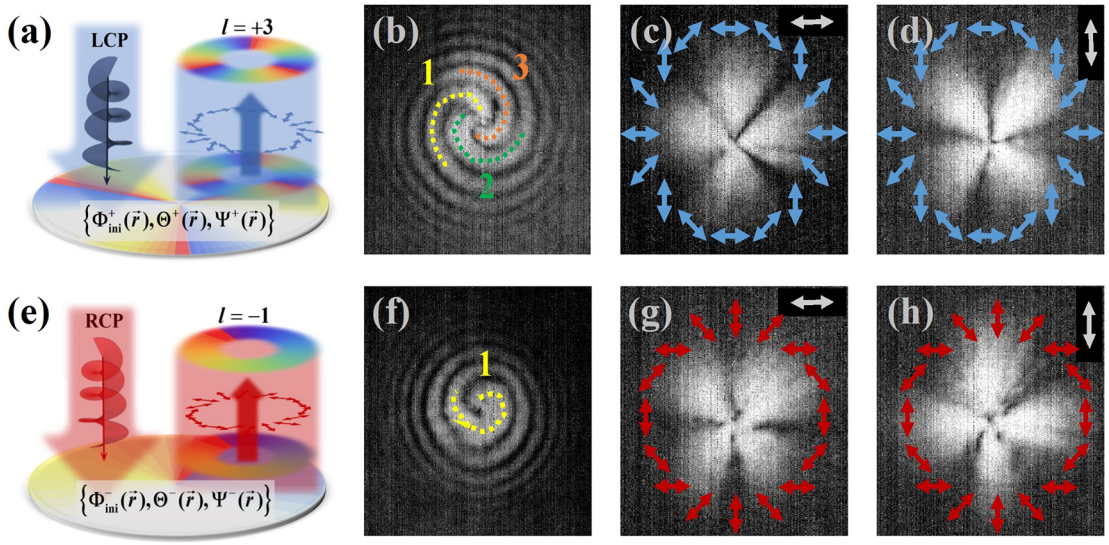

Figure 6: Experimental characterizations of metadevice II.
Schematics of light scatterings at a metadevice exhibiting $\{\Phi^{+}_{ini}, \Theta^{+}, \Psi^{+}\}$ and $\{\Phi^{-}_{ini}, \Theta^{-}, \Psi^{-}\}$ distributions as given by Eqs. (9) and (10), under illuminations of (a) left circular polarization (LCP) and (e) right circular polarization (RCP) incidences. Measured far-field interference patterns between a spherical reference wave and light beams reflected by metadevice II under (b) LCP and (f) RCP incidences, respectively. Far-field images recorded by our CCD with a linear polarizer placed in front of it, tilted by an angle of (c, g) 0° and (d, h) 90°, as metadevice II is illuminated by (c, d) LCP and (g, h) RCP incidences, respectively. Arrows in (c, d, g, h) illustrate the expected polarization patterns at different angles.

beams. Inferenced with a spherical wave, the resulting patterns show that now the reflected beam under LCP incidence exhibits an OAM with $l = +3$ (Figure 6b) while that under RCP incidence exhibits an OAM of $l = -1$ (Figure 6f), manifested by the opposite spiral direction as compared to Figure 5d. Meanwhile, Figures 6c, d, g, and h depict the measured intensity patterns of two reflected beams with a linear polarizer placed horizontally or vertically, respectively. Again, compared to those shown in Figure 5, here more intensity zeros appear in the measured patterns, at angles precisely consistent with the expected polarization distributions depicted in the figure. The working efficiency of our metadevice is numerically evaluated as 55% (see more details in Sec. 7 of SM). One can notice some image distortions in Figures 6b–h, which are caused by the material loss–induced stray light with undesired OAM and local polarization properties. Such issue reducing the working efficiency of metadevices could be solved by employing lossless meta-atom designs such as dielectric resonators.

We emphasize that the polarization distributions of the generated VOFs are not confined to those realized in Figure 6, but can in principle be rather general. Equations (2)–(4) reveal that the ellipticity distribution of polarization pattern (dictated by $\Theta^{+}(\vec{r})$) can be freely chosen, so that the local polarizations are not necessary LPs. Meanwhile, the distribution of local polar direction, dictated by the function $\Psi^{+}(\vec{r})$, can also change easily, although it is intimately linked with the two expected wave fronts via $\Psi^{+}(\vec{r}) = \Phi^{+}_{ini}(\vec{r}) - \Phi^{-}_{ini}(\vec{r}) - \pi/2$. Therefore, through tuning these functions $(\Theta^{+}(\vec{r}), \Psi^{+}(\vec{r}))$ we can readily design metadevices to realize highly nontrivial polarization distributions beyond the standard ones. As a particular example, we successfully retrieve the geometric parameters $\{L_u(\vec{r}), L_v(\vec{r}), \xi(\vec{r})\}$ of all needed meta-atoms to form a metadevice exhibiting the functionalities specified by Eqs. (5) and (6). The device layout is shown in Fig. S14 in SM. We have numerically studied the wave front and polarization properties of two VOFs generated by such a device, with realistic material losses fully taken into account. The computed results clearly verify our predictions that two generated VOFs indeed exhibit inhomogeneous distributions of elliptical polarizations dictated by the functions $(\Theta^{\pm}(\vec{r}), \Psi^{\pm}(\vec{r}))$ as specified in Eqs. (5) and (6) (see more details in Section 6 of SM). Such numerical calculations also well validate our design strategy established in Section 2 based on ideal meta-atoms.

3 Conclusions and perspectives

In short, we have established a generic strategy to design high-efficiency metadevices to bifunctionally create complex VOFs with desired wave fronts and polarization distributions, through exploring the full capabilities of meta-

atoms in controlling light polarizations and combining two different mechanisms (resonance phases and geometric phases) to generate phase shifts for incident light. Based on the established guidelines, we design and fabricate two metadevices working at telecom wavelengths and experimentally demonstrate their bifunctional generations of two vortex vectorial beams possessing different topological charges and distinct polarization distributions, as shined by CP light with different helicity.

Our results pave the road to generate complex VOFs with desired properties, which may inspire many future works on both fundamental and application sides of research. For example, switching the LCP and RCP incidences to two cross-polarized LP ones, the resulting VOFs generated by our devices, obtained by linear combinations of previous two, thus change accordingly. These new patterns not only provide more VOFs for potential applications but also make dynamical tuning of the VOFs possible. Moreover, generating VOFs with truly delinked properties and their optical characterizations are very interesting and challenging future works.

4 Materials and methods

4.1 Numerical simulations

We perform FDTD simulations using numerical software Concerto 7.0. The permittivity of Au is described by the Drude model $\varepsilon_r(\omega) = \varepsilon_\infty - \frac{\omega_p^2}{\omega(\omega+i\gamma)}$ with $\varepsilon_\infty = 9, \omega_p = 1.367 \times 10^{16}\,\mathrm{s}^{-1}, \gamma = 1.224 \times 10^{14}\,\mathrm{s}^{-1}$, obtained by fitting with experimental results. The SiO_2 spacer was considered as a lossless dielectric with permittivity $\varepsilon = 2.085$. Additional losses caused by surface roughness and grain boundary effects in thin films, as well as dielectric losses are effectively considered in fitting the parameter γ.

4.2 Sample fabrications

All samples were fabricated using standard thin-film deposition and electron-beam lithography (EBL) techniques. We firstly deposit 5-nm Cr, 125-nm Au, 5-nm Cr and a 100-nm SiO_2 dielectric layer onto a silicon substrate using magnetron DC-sputtering (Cr and Au) and RF-sputtering (SiO_2). Secondly, we lithographed the cross structures with EBL employing a ~100-nm-thick PMMA2 layer at an acceleration voltage of 20 keV. After development in a 1:3 solution of methyl isobutyl ketone and isopropyl alcohol, a 5-nm Cr adhesion layer and a 30-nm Au layer were deposited subsequently using thermos evaporation. The Au patterns were finally formed on top of the SiO_2 film after a lift-off process using acetone.

4.3 Experimental setup

We use a homemade NIR microimaging system equipped with an NIR CCD (NIRvana: 640-ST from Princeton Instruments) and an additional interference optical path to characterize the performances of our metadevices. A broadband supercontinuum laser source and a fiber-coupled grating spectrometer (ideaoptics NIR2500) were used in far-field measurement. Beam splitter, linear polarizer, and visible CCD are also used to measure the reflectance and analyze the polarization distributions. More details can be found in SM.

Acknowledgements: This work was funded by National Natural Science Foundation of China (No. 11734007, No. 91850101, No. 11674068 and No. 11874118), National Key Research and Development Program of China (No. 2017YFA0303504 and No. 2017YFA0700201), Natural Science Foundation of Shanghai (No. 20JC1414601 and No.18ZR1403400), Fudan University-CIOMP Joint Fund (No. FC2018-006). L. Zhou and Q. He acknowledge technical supports from the Fudan Nanofabrication Laboratory for sample fabrications.

Author contribution: D.W., T.L. and Y.Z. contributed equally to this work. D.W. carried out simulations, fabricated the samples and conducted part of the measurements; T.L. did the theoretical calculations and designed the samples; Y.Z. and X.Z. built the experimental setup and conducted part of measurements; S.S. provided technical supports for simulations and data analyses. L.Z. and Q.H. conceived the idea and supervised the project. All the authors contributed to the preparation of the manuscript, and have accepted responsibility for the entire content of this submitted manuscript and approved submission.

Research funding: This work was funded by National Natural Science Foundation of China (No. 11734007, No. 91850101, No. 11674068, No. 11874118), National Key Research and Development Program of China (No. 2017YFA0303504 and No. 2017YFA0700201), Natural Science Foundation of Shanghai (No. 20JC1414601 and No.18ZR1403400), Fudan University-CIOMP Joint Fund (No. FC2018-006).

Conflict of interest statement: The authors declare no conflict of interest.

References

[1] D. G. Hall, "Vector-beam solutions of Maxwell's wave equation," *Opt. Lett.*, vol. 21, no. 1, p. 9, 1996.

[2] Q. Zhan, "Cylindrical vector beams: from mathematical concepts to applications," *Adv. Opt. Photonics*, vol. 1, no. 1, p. 1, 2009.

[3] J. Chen, C. Wan, and Q. Zhan, "Vectorial optical fields: recent advances and future prospects," *Sci. Bull.*, vol. 63, no. 1, pp. 54–74, 2018.
[4] A. S. Ostrovsky, C. Rickenstorff-Parrao, and V. Arrizón, "Generation of the "perfect" optical vortex using a liquid-crystal spatial light modulator," *Opt. Lett.*, vol. 38, no. 4, p. 534, 2013.
[5] P. Chen, W. Ji, B. Y. Wei, W. Hu, V. Chigrinov, and Y. Q. Lu, "Generation of arbitrary vector beams with liquid crystal polarization converters and vector-photoaligned q-plates," *Appl. Phys. Lett.*, vol. 107, no. 24, 2015. https://doi.org/10.1063/1.4937592.
[6] Z. Liu, Y. Liu, Y. Ke, et al., "Generation of arbitrary vector vortex beams on hybrid-order Poincaré sphere," *Photonics Res.*, vol. 5, no. 1, p. 15, 2017.
[7] N. Yu and F. Capasso, "Flat optics with designer metasurfaces," *Nat. Mater.*, vol. 13, no. 2, pp. 139–150, 2014.
[8] Q. He, S. Sun, S. Xiao, and L. Zhou, "High-efficiency metasurfaces: principles, realizations, and applications," *Adv. Opt. Mater.*, vol. 6, no. 19, p. 1800415, 2018.
[9] S. Sun, Q. He, J. Hao, S. Xiao, and L. Zhou, "Electromagnetic metasurfaces: physics and applications," *Adv. Opt. Photonics*, vol. 11, no. 2, p. 380, 2019.
[10] J. Hao, Y. Yuan, L. Ran, et al., "Manipulating electromagnetic wave polarizations by anisotropic metamaterials," *Phys. Rev. Lett.*, vol. 99, no. 6, p. 063908, 2007.
[11] S. Jiang, X. Xiong, Y.-S. Hu, et al., "Controlling the polarization state of light with a dispersion-free metastructure," *Phys. Rev. X*, vol. 4, no. 2, p. 021026, 2014.
[12] J. P. Balthasar Mueller, N. A. Rubin, R. C. Devlin, B. Groever, and F. Capasso, "Metasurface polarization optics: independent phase control of arbitrary orthogonal states of polarization," *Phys. Rev. Lett.*, vol. 118, no. 11, p. 113901, 2017.
[13] N. Yu, P. Genevet, M. A. Kats, et al., "Light propagation with phase discontinuities: generalized laws of reflection and refraction," *Science*, vol. 334, no. 6054, pp. 333–337, 2011.
[14] X. Ni, N. K. Emani, A. V. Kildishev, A. Boltasseva, and V. M. Shalaev, "Broadband light bending with plasmonic nanoantennas," *Science*, vol. 335, no. 6067, p. 427, 2012.
[15] S. Sun, Q. He, S. Xiao, Q. Xu, X. Li, and L. Zhou, "Gradient-index meta-surfaces as a bridge linking propagating waves and surface waves," *Nat. Mater.*, vol. 11, no. 5, pp. 426–431, 2012.
[16] S. Sun, K. Y. Yang, C. M. Wang, et al., "High-efficiency broadband anomalous reflection by gradient meta-surfaces," *Nano Lett.*, vol. 12, no. 12, pp. 6223–6229, 2012.
[17] L. Huang, X. Chen, H. Mühlenbernd, et al., "Dispersionless phase discontinuities for controlling light propagation", *Nano Lett*, vol. 12, 5750–5755, 2012.
[18] A. Arbabi, Y. Horie, M. Bagheri, and A. Faraon, "Dielectric metasurfaces for complete control of phase and polarization with subwavelength spatial resolution and high transmission," *Nat. Nanotechnol.*, vol. 10, no. 11, pp. 937–943, 2015.
[19] T. Cai, S. W. Tang, G. M. Wang, et al., "High-Performance bifunctional metasurfaces in transmission and reflection geometries," *Adv. Opt. Mater.*, vol. 5, p. 1600506, 2017.
[20] X. Li, S. Xiao, B. Cai, Q. He, T. J. Cui, and L. Zhou, "Flat metasurfaces to focus electromagnetic waves in reflection geometry," *Opt. Lett.*, vol. 37, no. 23, p. 4940, 2012.
[21] M. Khorasaninejad, W. T. Chen, R. C. Devlin, J. Oh, A. Y. Zhu, and F. Capasso, "Metalenses at visible wavelengths: diffraction-limited focusing and subwavelength resolution imaging," *Science*, vol. 352, no. 6290, pp. 1190–1194, 2016.
[22] S. Wang, P. C. Wu, V.-C. Su, et al., "A broadband achromatic metalens in the visible," *Nat. Nanotechnol.*, vol. 13, no. 3, pp. 227–232, 2018.
[23] Z.-B. Fan, Z.-K. Shao, M.-Y. Xie, et al., "Silicon nitride metalenses for close-to-one numerical aperture and wide-angle visible imaging," *Phys. Rev. Appl.*, vol. 10, no. 1, p. 014005, 2018.
[24] W. T. Chen, K.-Y. Y. Yang, C.-M. M. Wang, et al., "High-efficiency broadband meta-hologram with polarization-controlled dual images," *Nano Lett.*, vol. 14, no. 1, pp. 225–230, 2014.
[25] G. Zheng, H. Mühlenbernd, M. Kenney, G. Li, T. Zentgraf, and S. Zhang, "Metasurface holograms reaching 80% efficiency," *Nat. Nanotechnol.*, vol. 10, pp. 308–312, 2015.
[26] B. Wang, F. Dong, Q.-T. T. Li, et al., "Visible-frequency dielectric metasurfaces for multiwavelength Achromatic and highly dispersive holograms," *Nano Lett.*, vol. 16, no. 8, pp. 5235–5240, 2016.
[27] L. Wang, S. Kruk, H. Tang, et al., "Grayscale transparent metasurface holograms," *Optica*, vol. 3, no. 12, p. 1504, 2016.
[28] N. Yu, F. Aieta, P. Genevet, M. a Kats, Z. Gaburro, and F. Capasso, "A broadband, background-free quarter-wave plate based on plasmonic metasurfaces," *Nano Lett.*, vol. 12, no. 12, pp. 6328–6333, 2012.
[29] H. Zhou, B. Sain, Y. Wang, et al., "Polarization-encrypted orbital angular momentum multiplexed metasurface holography," *ACS Nano*, vol. 14, no. 5, pp. 5553–5559, 2020.
[30] J. T. Heiden, F. Ding, J. Linnet, Y. Yang, J. Beermann, and S. I. Bozhevolnyi, "Gap-surface plasmon metasurfaces for broadband circular-to-linear polarization conversion and vector vortex beam generation," *Adv. Opt. Mater.*, vol. 7, no. 9, p. 1801414, 2019.
[31] F. Ding, Y. Chen, and S. I. Bozhevolnyi, "Focused vortex-beam generation using gap-surface plasmon metasurfaces," *Nanophotonics*, vol. 9, no. 2, pp. 371–378, 2020.
[32] N. K. Grady, J. E. Heyes, D. R. Chowdhury, et al., "Terahertz metamaterials for linear polarization conversion and anomalous refraction," *Science*, vol. 340, no. 6138, pp. 1304–7, 2013.
[33] S. Li, Z. Wang, S. Dong, et al., "Helicity-delinked manipulations on surface waves and propagating waves by metasurfaces," *Nanophotonics*, vol. 9, p. 3473, 2020.
[34] E. Wang, J. Niu, Y. Liang, et al., "Complete control of multichannel, angle-multiplexed, and arbitrary spatially varying polarization fields," *Adv. Opt. Mater.*, vol. 8, no. 6, p. 1901674, 2020.
[35] Y. Xu, Q. Li, X. X. Zhang, et al., "Spin-Decoupled multifunctional metasurface for asymmetric polarization generation," *ACS Photonics*, vol. 6, no. 11, pp. 2933–2941, 2019.
[36] Z. Deng, M. Jin, X. Ye, et al., "Full-color complex-amplitude vectorial holograms based on multi-freedom metasurfaces," *Adv. Funct. Mater.*, vol. 30, no. 21, p. 1910610, 2020.
[37] E. Maguid, I. Yulevich, M. Yannai, V. Kleiner, M. L. Brongersma, and E. Hasman, "Multifunctional interleaved geometric-phase dielectric metasurfaces," *Light Sci. Appl.*, vol. 6, no. 8, p. e17027, 2017.
[38] Y. Yang, W. Wang, P. Moitra, I. I. Kravchenko, D. P. Briggs, and J. Valentine, "Dielectric meta-reflectarray for broadband linear polarization conversion and optical vortex generation," *Nano Lett.*, vol. 14, no. 3, pp. 1394–1399, 2014.

[39] G. Ding, K. Chen, X. Luo, J. Zhao, T. Jiang, and Y. Feng, "Dual-helicity decoupled coding metasurface for independent spin-to-orbital angular momentum conversion," *Phys. Rev. Appl.*, vol. 11, no. 4, p. 044043, 2019.
[40] H. Zhao, B. Quan, X. Wang, C. Gu, J. Li, and Y. Zhang, "Demonstration of orbital angular momentum multiplexing and demultiplexing based on a metasurface in the terahertz band," *ACS Photonics*, vol. 5, no. 5, pp. 1726–1732, 2018.
[41] F. Yue, D. Wen, C. Zhang, et al., "Multichannel polarization-controllable superpositions of orbital angular momentum states," *Adv. Mater.*, vol. 29, no. 15, p. 1603838, 2017.
[42] F. Yue, D. Wen, J. Xin, B. D. Gerardot, J. Li, and X. Chen, "Vector vortex beam generation with a single plasmonic metasurface," *ACS Photonics*, vol. 3, no. 9, pp. 1558–1563, 2016.
[43] S. Kruk, B. Hopkins, I. I. Kravchenko, A. Miroshnichenko, D. N. Neshev, and Y. S. Kivshar, "Broadband highly efficient dielectric metadevices for polarization control," *APL Photonics*, vol. 1, no. 3, p. 030801, 2016.
[44] E. Arbabi, S. M. Kamali, A. Arbabi, and A. Faraon, "Vectorial holograms with a dielectric metasurface: ultimate polarization pattern generation," *ACS Photonics*, vol. 6, no. 11, pp. 2712–2718, 2019.
[45] F. Ding, Y. Chen, Y. Yang, and S. I. Bozhevolnyi, "Multifunctional metamirrors for broadband focused vector-beam generation," *Adv. Opt. Mater.*, vol. 7, no. 22, p. 1900724, 2019.
[46] Y. Xu, H. Zhang, Q. Li, et al., "Generation of terahertz vector beams using dielectric metasurfaces via spin-decoupled phase control," *Nanophotonics*, vol. 9, p. 3393, 2020.
[47] M. Jia, Z. Wang, H. Li, et al., "Efficient manipulations of circularly polarized terahertz waves with transmissive metasurfaces," *Light Sci. Appl.*, vol. 8, no. 1, p. 16, 2019.
[48] W. Luo, S. Xiao, Q. He, S. Sun, and L. Zhou, "Photonic spin Hall effect with nearly 100% efficiency," *Adv. Opt. Mater.*, vol. 3, no. 8, pp. 1102–1108, 2015.
[49] S. Ma, X. Wang, W. Luo, et al., "Ultra-wide band reflective metamaterial wave plates for terahertz waves," *Europhys. Lett.*, vol. 117, no. 3, p. 37007, 2017.
[50] S. Wang and Q. Zhan, "Reflection type metasurface designed for high efficiency vectorial field generation," *Sci. Rep.*, vol. 6, p. 29626, 2016.
[51] H. X. Xu, L. Han, Y. Li, et al., "Completely spin-decoupled dual-phase hybrid metasurfaces for arbitrary wavefront control," *ACS Photonics*, vol. 6, p. 211, 2019.
[52] Z. Wang, S. Li, X. Zhang, et al., "Excite spoof surface plasmons with tailored wavefronts using high-efficiency terahertz metasurfaces," *Adv. Sci.*, p. 2000982, 2020. https://doi.org/10.1002/advs.202000982.
[53] S. Pancharatnam, "Generalized theory of interference and its applications," *Proc. Indian Acad. Sci. Sect. A*, vol. 44, no. 6, p. 398, 1956.
[54] M. V. Berry, "Quantal phase factors accompanying adiabatic changes," *Proc. R. Soc. A Math. Phys. Eng. Sci.*, vol. 392, no. 1802, pp. 45–57, 1984.
[55] Z. Bomzon, G. Biener, V. Kleiner, and E. Hasman, "Space-variant Pancharatnam–Berry phase optical elements with computer-generated subwavelength gratings," *Opt. Lett.*, vol. 27, no. 13, p. 1141, 2002.
[56] W. Luo, S. Sun, H.-X. Xu, Q. He, and L. Zhou, "Transmissive ultrathin Pancharatnam–Berry metasurfaces with nearly 100% efficiency," *Phys. Rev. Appl.*, vol. 7, no. 4, p. 044033, 2017.
[57] C. Qu, S. Ma, J. Hao, et al., "Tailor the functionalities of metasurfaces based on a complete phase diagram," *Phys. Rev. Lett.*, vol. 115, no. 23, p. 235503, 2015.

Supplementary Material: The online version of this article offers supplementary material (https://doi.org/10.1515/nanoph-2020-0465).